nature energy

Article

https://doi.org/10.1038/s41560-023-01255-2

Silicon heterojunction solar cells with up to 26.81% efficiency achieved by electrically optimized nanocrystalline-silicon hole contact layers

Received: 21 December 2022

Accepted: 24 March 2023

Published online: 4 May 2023

Check for updates

Hao Lin[1,2,4], Miao Yang[1,4], Xiaoning Ru[1,4], Genshun Wang[1,2], Shi Yin[1] ✉, Fuguo Peng[1], Chengjian Hong[1], Minghao Qu[1], Junxiong Lu[1], Liang Fang[1], Can Han[2,3], Paul Procel[3], Olindo Isabella[3], Pingqi Gao[2] ✉, Zhenguo Li[1] & Xixiang Xu[1] ✉

Silicon heterojunction (SHJ) solar cells have reached high power conversion efficiency owing to their effective passivating contact structures. Improvements in the optoelectronic properties of these contacts can enable higher device efficiency, thus further consolidating the commercial potential of SHJ technology. Here we increase the efficiency of back junction SHJ solar cells with improved back contacts consisting of p-type doped nanocrystalline silicon and a transparent conductive oxide with a low sheet resistance. The electrical properties of the hole-selective contact are analysed and compared with a p-type doped amorphous silicon contact. We demonstrate improvement in the charge carrier transport and a low contact resistivity (<5 mΩ cm^2). Eventually, we report a series of certified power conversion efficiencies of up to 26.81% and fill factors up to 86.59% on industry-grade silicon wafers (274 cm^2, M6 size).

Photovoltaic (PV) solar cells are one of the main renewable energy sources with zero operating carbon emissions; driven by ambitious carbon neutral policies worldwide, they are quickly becoming a mainstream energy supply. To a large extent, power conversion efficiency (PCE) determines whether a PV technology is competitive. Wafer-based crystalline silicon (c-Si) solar cells are the dominant technology in the global PV market. Aiming at a higher PCE, technology iteration is occurring from the passivated emitter and rear cell (PERC) to tunnel oxide passivated contact (TOPCon) and silicon heterojunction (SHJ) solar cells[1–7].

SHJ technology employs an n-type (p-type) doped hydrogenated amorphous silicon (a-Si:H) layer, called n-a-Si:H (p-a-Si:H), as the electron-selective contact layer (ESC)–hole-selective contact layer (HSC). This overlays the intrinsic hydrogenated amorphous silicon (i-a-Si:H) layer, providing high-quality chemical passivation and minimizing the deficit in open circuit voltage (V_{OC})[8–13]. The electrical performance of the solar cells depends strongly on the net doping of both the ESC and HSC layers. This is particularly relevant to the HSC layer, which is the emitter in SHJ solar cells based on n-type wafers. A sufficiently high doping concentration produces favourable band bending, allowing holes (minority carriers) to tunnel (selective collection of holes); efficient field-effect passivation, repelling electrons from the interface and mitigating the resulting interface recombination; and a reduced energy barrier when directly in contact with the n-type transparent conducting oxide (TCO)[14–16]. However, doped a-Si:H layers are always limited by unsatisfying electrical conductivity ($\sigma < 10^{-4}$ S cm^{-1})

[1]LONGi Central R&D Institute, LONGi Green Energy Technology Co., Ltd., Xi'an, China. [2]School of Materials, Institute for Solar Energy Systems, Sun Yat-sen University, Guangzhou, China. [3]Photovoltaic Materials and Devices Group, Delft University of Technology, Delft, the Netherlands. [4]These authors contributed equally: Hao Lin, Miao Yang, Xiaoning Ru. ✉e-mail: yinshi@longi.com; gaopq3@mail.sysu.edu.cn; xuxixiang@longi.com

and relatively high activation energy (E_a > 250 meV), which cause high contact resistivity in SHJ solar cells[17–20].

In contrast to defect-rich amorphous silicon, hydrogenated nanocrystalline silicon (nc-Si:H) dramatically improves film crystallinity, which straightforwardly favours the improvement of carrier mobility and effective doping concentration. However, depositing a sufficiently thin layer of highly crystalline nc-Si:H on amorphous surfaces at low temperature is challenging. Depositing p-type doped nc-Si:H (p-nc-Si:H) is even more difficult, as boron doping restricts grain growth. Sophisticated techniques from deposition engineering, including pretreatment methods, adjusting deposition parameters (pressure, temperature, power, frequency and silane dilution) and post-treatment, help to address these issues[21–25]. For example, researchers discovered that CO_2 treatment facilitates fast nucleation for the growth of nanocrystalline silicon film[26]. High crystalline volume fraction (X_C)—up to 50%—has been reported by several groups through fine-tuning gas flow rates[21,25]. Umishio et al.[27] found a clear relation between the nanostructure evolution of the p-nc-Si:H layers and their electrical properties and resulting performance. They concluded that surface coalescence of the p-nc-Si:H nanocrystals, rather than doping concentration, dominantly determines the E_a of the film[27]. In other words, hole selectivity and hole transport through the TCO–p-nc-Si:H contact and hence, the solar cell's V_{OC} and fill factor (FF) are crucially influenced by the electrical contact properties between TCO and the crystalline phase at the surface of the p-nc-Si:H layer[19]. Based on this understanding, the contact resistivity of p-nc-Si:H-based HSCs has been reduced to about 100 mΩ cm^2, yielding a series resistance (R_S) of 0.65–1.3 Ω cm^2 and a 23–25% PCE (Supplementary Table 1)[27–31]. Nevertheless, realizing the advantageous electrical properties of SHJ solar cells over their TOPCon counterparts still poses a challenge, and the opportunity to unlock the full potential of SHJ technology remains open.

In this contribution, we report the successful introduction of nanocrystallization processes for fabricating cutting-edge HSCs, which—when paired with correspondingly tailored TCO—result in improved PCEs and FFs on wafer-scale single-junction SHJ solar cells. We demonstrate a 26.30% SHJ solar cell with an FF of 86.59%; to the best of our knowledge, this FF outperforms any other silicon solar cell. By reducing the shading ratio from 2.8 to 2.0% and modifying the window layers at the front to minimize the parasitic absorption, we further boost the PCE to 26.74% by increasing the short-circuit current density (J_{SC}) to 41.16 mA cm^{-2}. Finally, by introducing an additional reflective MgF_2/Ag stack at the rear side and regulating the transmittance of TCO, we achieve a PCE of 26.81% with a J_{SC} of 41.45 mA cm^{-2}. Investigation of the power and series resistance losses reveals outstanding performance of these HSCs, with reduced contact resistivity (ρ_c < 5 mΩ cm^2) and improved passivation (recombination current density J_0 = 0.5 fA cm^{-2}). Structural and electrical characterizations of the p-nc-Si:H indicate high X_C (63%), ultralow E_a (<115 meV) and excellent σ (>3 S cm^{-1}), which is four orders of magnitude higher than that of the traditional p-a-Si:H film[32,33]. HSCs endowed with these electrical improvements easily trigger band-to-band tunnelling (BTBT) transport behaviour and induce a sharp band bending, enhancing hole extraction efficiency.

Efficiency increase analysis of SHJ solar cells

In mass production, the competition between SHJ and TOPCon technologies is fierce. As can be seen from Fig. 1a, SHJ solar cells feature greater electrical performance measured by V_{OC} × FF, while TOPCon and PERC hold relatively superior J_{SC}. The inferior J_{SC} of SHJ solar cells can be attributed to the strong parasitic absorption inherent in the functional layers at the front side; PERC and TOPCon usually yield higher J_{SC} (>41 mA cm^{-2}) due to the use of conventionally diffused front junctions and optically transparent antireflective coatings[34]. Benefiting from the unique design of rear-sided passivating contact with an SiO_x/poly-Si(n$^+$) stack, TOPCon wins out over PERC with intrinsically improved V_{OC} (ref. 35). SHJ produces the highest V_{OC} among the c-Si solar cell technologies because of the excellent surface passivation provided by the i-a-Si:H layers. Figure 1b illustrates the FF versus V_{OC} of different solar cell technologies, in which one can clearly see the superior FF of SHJ solar cells as compared with that of PERC and TOPCon devices.

In Fig. 1b, the lines corresponding to the Green limits[36] for different ideal factors (n) are indicated as well. The value of the ideality factor of a c-Si cell is based on the recombination mechanism: n = 2/3 for Auger recombination and n = 1 for Shockley–Read–Hall (SRH) and band-to-band recombination at low injection level. Combining high-quality c-Si wafers with the superior surface passivation we obtained, the intrinsic recombination of SHJ solar cells becomes dominant. In the case of Auger recombination at high injection level, the ideality factor value of our SHJ cells is found to be lower than one. The reduction in ideality factor causes a more square shape in the J–V curve, leading to a remarkable improvement in FF.

As indicated in Fig. 1, the performance of SHJ solar cells has increased almost linearly both electrically and optically. The first SHJ solar cell from our group (LONGi) delivered a PCE of 25.26% (ref. 37), and we have now further boosted all the PV parameters. In this work, we show a PCE of 26.81%, with V_{OC} of 751.4 mV (an improvement of 2.9 mV), FF of 86.07% (0.57% improvement) and J_{SC} of 41.45 mA cm^{-2} (an improvement of 1.97 mA cm^{-2}), an overall efficiency gain of 1.55%. Note that we achieved the highest FF of 86.59% on a different device: that is, the cell delivering an efficiency of 26.30%. Theoretical predictions yield a similar trend, as shown by the blue to red gradient solid line in Fig. 1b. Radiative, Auger and surface recombinations were taken into consideration in the calculation, while additional R_S and shunt resistance (R_{sh}) were not included. The improvement of LONGi's SHJ solar cells follows the overall tendency apart from small deviations in practical and calculated FF, which are mainly attributed to the advance in reduction of R_S. Note that the measurement approach (Methods) excludes some R_S components, such as the resistance of the grid at the rear side and of the bus bars at the front side. We found that ultrahigh FF only occurs at extremely low R_S and furthermore, requires high-quality passivation: that is, high V_{OC}. This is why LONGi SHJ solar cells possess a prominent advantage in electrical performance (V_{OC} × FF) (Fig. 1a) over PERC and TOPCon cells. Limited by insufficient passivation, the positive effect of reduced R_S on FF cannot be fully unlocked for PERC and TOPCon cells.

To reveal the main contributions to the efficiency increase, two related designs with p-a-Si:H (cell 1, 25.26% PCE) and p-nc-Si:H (cell 2, 26.30%) serving as the rear emitter are investigated with the Quokka2 software[38,39]. For the sake of simplicity, hereafter we name cell 1 and cell 2 as p-a-Si:H cell and p-nc-Si:H cell, respectively. Numerical simulations and fits to experimental data of R_S and power loss analysis (PLA) are shown in Fig. 2. Figure 2a shows the structure of the LONGi SHJ solar cells; the parameter variations between the p-a-Si:H cell and p-nc-Si:H cell are listed in Supplementary Table 3. The two devices are in a front and back contact architecture on an n-type c-Si (n-Si) wafer with front-sided n-type nanocrystalline silicon oxide (n-nc-SiO_x:H) and a back junction (BJ). Using BJ structure alleviates the electrical requirements on the front-side TCO and metal electrodes since a large portion of the majority carriers (electrons) can be laterally collected via the n-Si wafer absorber[40]. The main difference between the two solar cells comes from the BJ stacks; the p-nc-Si:H cell features p-nc-Si:H and a tailored TCO with a sheet resistance of 40 Ω per sqaure, while the p-a-Si:H cell features p-a-Si:H and a TCO with a sheet resistance of 80 Ω per square. Due to the excellent σ and E_a of p-nc-Si:H, the rear contact resistivity is reduced, which will be discussed in the next section.

Figure 2b,c shows the experimental and fitted J–V curves of their related cells. The experimental curves include the real-light J–V curve (blue triangles) and the pseudo-light J–V curve tested by a Suns–V_{OC} measurement (blue circles). The fitted J–V curves were simulated by Quokka2 (refs. 38,39). Input parameters were determined

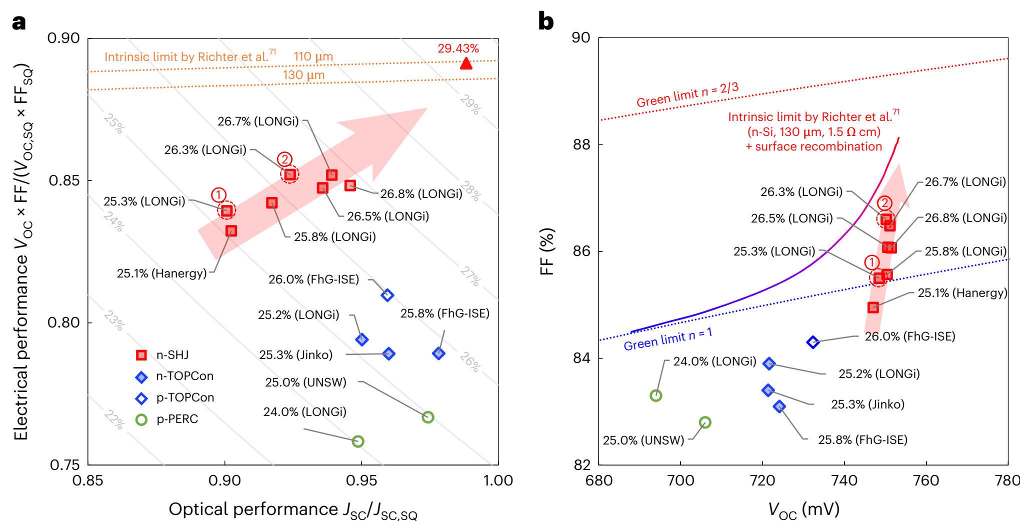

Fig. 1 | Comparison of PV parameters of high-efficiency silicon solar cells. **a**, Measured PCEs of different high-performance c-Si solar cell technologies, including n-type wafer SHJ solar cells (n-SHJ) reported by LONGi and Hanergy, TOPCon solar cells reported by LONGi, Jinko and Fraunhofer ISE (FhG-ISE) and PERC solar cells based on p-type wafer (p-PERC) reported by LONGi and University of New South Wales (UNSW), overlaid on efficiency curves as a function of electrical (V_{OC} × FF) and optical (J_{SC}) performances and normalized by the Shockley–Queisser (SQ) limit of a c-Si cell under standard test conditions. The raw data are provided in Supplementary Table 2. The upper limits of the electrical contribution and Richter limit as a function of J_{SC} are shown for wafer thicknesses of 130 μm (the wafer thickness of SHJ solar cells in this paper) and 110 μm (the ideal wafer thickness for approaching the theoretical limiting efficiency of 29.43%)[65,71]. **b**, Detailed distributions of measured PCEs of different high-performance c-Si solar cell technologies as a function of V_{OC} and FF. The Green limit[36] with ideality factor n = 2/3 (n = 1), assuming a one-diode model and without considering the effects of R_S and R_{sh}, is drawn with a blue (red) dotted line. The blue to red gradient solid line is derived by theoretical calculation (same as the calculation in Supplementary Fig. 1) contributed from only intrinsic and surface recombination for devices with n-Si wafers of 130 μm thick and 1.5 Ω cm resistivity. The red arrows indicate the trend towards improved efficiency in SHJ solar cells over time. LONGi cells with typical SHJ design and p-a-Si:H (p-nc-Si:H) as the rear emitter are indicated by 1 (2).

by the measured sheet resistance of the TCO, the line resistance of the finger, the contact resistivity and recombination of the heterojunction. A full description of these parameters is in Supplementary Table 4. For comparison, the corresponding intrinsic light J–V curves computed from the theoretical limit in electrical performance are also shown (grey lines). Observe that the deviation between the Suns–V_{OC} curve and the light J–V curve (arrows enclosed by black circles) differs between the p-a-Si:H cell and the p-nc-Si:H cell. To explain this, note that we can define a pseudo-fill factor (pFF) from a Suns–V_{OC} curve ignoring all resistance. Both the p-a-Si:H cell and p-nc-Si:H cell have similar pFF values, which means that the difference in FF at the maximum power point (MPP) originates from a difference in the series resistance R_S. Therefore, a smaller gap between the light and pseudo-light J–V curves in the p-nc-Si:H cell indicates a smaller R_S.

To explore how the record FF of 86.59% was achieved, we fit the J–V curves in Fig. 2b,c to determine power loss and series resistance, seen in Fig. 2d. The losses are divided into three regions: front ESC, bulk silicon (bulk) and rear HSC. Figure 2d also shows the series resistance determined from the power loss at MPP. From the p-a-Si:H cell to p-nc-Si:H cell, the total electrical power loss is reduced from 0.41 to 0.13 mW cm^{-2} at the rear HSC alone; this is nearly equal to the full power loss reduction, 0.3 mW cm^{-2} (from 1.01 to 0.71 mW cm^{-2}). This indicates that the improvement in electrical performance comes primarily from the rear HSC (as expected). In particular, the reduction of power loss at the rear HSC is attributed to the use of p-nc-Si:H and the updated TCO, which facilitates excellent passivation and contact performance. The series resistance analysis shows the same trend as the PLA. The total R_S is reduced from 381 mΩ cm^2 for the p-a-Si:H cell to 206 mΩ cm^2 for the p-nc-Si:H cell (Supplementary Fig. 2a); this difference mostly appears at the rear HSC, at which R_S is reduced from more than 130 mΩ cm^2 to less than 20 mΩ cm^2 (Fig. 2d). The slightly increased power loss in the bulk seen in the p-nc-Si:H cell could be caused by a small fluctuation in wafer quality. A slightly reduced R_S of the front ESC (from 47 to 41 mΩ cm^2) lies in the reduction of the sheet resistance of front TCO from ~150 to ~50 Ω per square. Note that to ensure the credibility of the R_S data, we measured the total R_S at MPP with four different methods[41], obtaining R_S = 353–381 mΩ cm^2 (p-a-Si:H cell) and 175–206 mΩ cm^2 (p-nc-Si:H cell), as shown in Supplementary Fig. 2b.

Characterization of p-nc-Si:H

As discussed above, the implementation of p-nc-Si:H together with matched TCO leads to a dramatic reduction in the contact resistivity at the rear side, resulting in an efficiency increase to 26.30%. As this contact, the overall resistance depends mainly on the bulk resistance of p-nc-Si:H itself and on the contact resistivity at the p-nc-Si:H–TCO interface. Therefore, gaining the optimal p-nc-Si:H layer is of critical importance to achieve high-efficiency SHJ solar cells. We investigated p-nc-Si:H layers grown from different recipes; corresponding deposition conditions and characterization results are elaborated in Fig. 3 and Supplementary Table 5. We studied the structural properties of the p-a-Si:H and p-nc-Si:H layers by both Raman spectroscopy and transmission electron microscopy (TEM). The Raman measurement was carried out with a 325-nm laser and performed on the p-a-Si:H or p-nc-Si:H layer deposited on a planar i-a-Si:H–glass substrate. The deposition process was identical to that of the fabrication procedure for solar cells. The Raman spectra were fitted with multiple (or single) Gaussian functions, as shown in Fig. 3a. For p-nc-Si:H, three Gaussian peaks are identified with the centres at 482, 507 and 518 cm^{-1}, representing separately the transverse optical phonon mode of amorphous silicon and two optical vibrational modes of nanocrystalline silicon[42,43]. In contrast, only one peak at 478 cm^{-1} is observed for p-a-Si:H, indicating a fully amorphous structure. X_C is determined from the integrated intensities (I) of the Gaussian peaks via equation (1) as follows[44,45]:

$$X_C = \frac{I_{510\,\mathrm{cm}^{-1}} + I_{520\,\mathrm{cm}^{-1}}}{\beta I_{480\,\mathrm{cm}^{-1}} + I_{510\,\mathrm{cm}^{-1}} + I_{520\,\mathrm{cm}^{-1}}}, \quad (1)$$

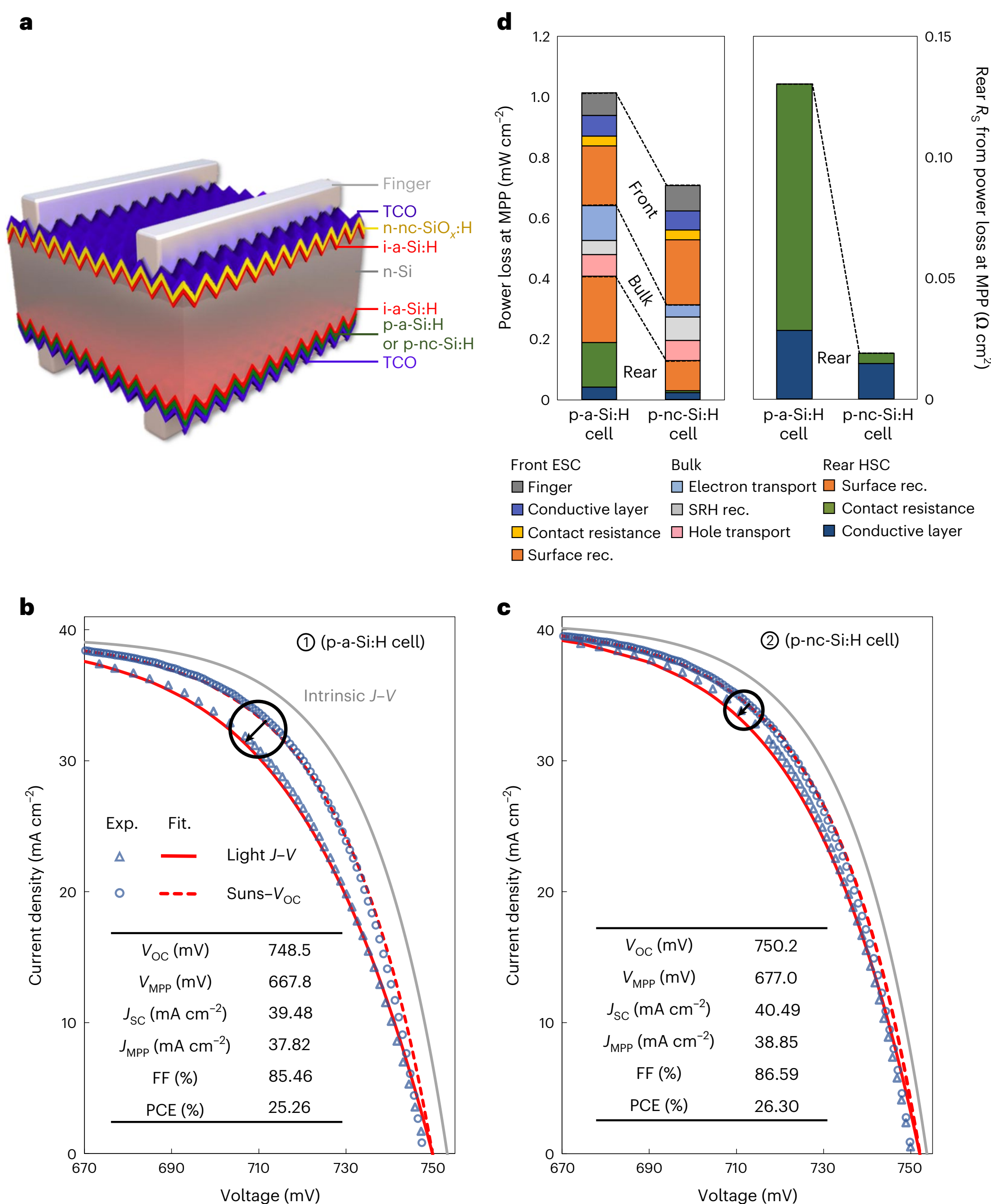

Fig. 2 | Electrical performance of LONGi SHJ solar cells with different designs. **a**, Diagram of LONGi SHJ solar cells. **b**,**c**, Experimental (Exp.) and fitted (Fit.) *J*–*V* curves for the p-a-Si:H cell (**b**, cell 1 in Fig. 1) and the p-nc-Si:H cell (**c**, cell 2 in Fig. 1). The fitted curves are derived from the Quokka2 simulations (Methods). Intrinsic *J*–*V* curves are obtained according to the Richter et al. model of intrinsic recombination with photon recycling (photon recycling coefficient of 0.6)[65,71]. The black arrows between the Suns–V_{OC} and light *J*–*V* curves indicate the series resistance of solar cells. Insets: the PV parameters certified by ISFH. **d**, PLA and corresponding R_S at the MPP derived by fitting *J*–*V* curves in **b** and **c**; rec, recombination. The loss of intrinsic recombination is not shown, and only the R_S at the rear is analysed. For a full analysis of R_S, see Supplementary Fig. 2a.

where $\beta = 0.8$ represents the ratio of the back-scattering cross-sections[46]. For the p-nc-Si:H sample, an X_C of 63% is obtained.

The cross-sectional TEM images of the HSCs based on p-a-Si:H and p-nc-Si:H are shown in Fig. 3b,c. The samples, namely TCO–p-nc-Si:H–i-a-Si:H–n-Si and TCO–p-a-Si:H–i-a-Si:H–n-Si, were taken by focused ion beam from as-prepared SHJ solar cells. In the TEM images, each layer in the stack is identified by its thickness, which was individually measured and confirmed by ellipsometry. In both samples, the thickness of the i-a-Si:H layer is almost same (about 6 nm), while the p-nc-Si:H layer (about 21 nm) is much thicker than that of p-a-Si:H (about 5 nm). A thicker p-nc-Si:H layer is required for incubation and for the subsequent phase transition from amorphous to crystalline. The higher X_C of the p-nc-Si:H layer is evidenced by the observation that nanocrystalline domains embedded in an amorphous phase coalesce laterally to one another. No crystalline feature is observed in the i-a-Si:H and p-a-Si:H layers. To identify nanocrystalline domains, fast Fourier transforms (FFTs) were performed on the TEM images (insets in Fig. 3b,c). In both samples, the reciprocal spots derived from the c-Si substrate are highlighted by red circles; these include high-order spots. In the p-nc-Si:H sample, additional reciprocal spots derived from nanocrystalline domains can be seen. We performed inverse FFT calculations on the FFT images, masking selected reciprocal spots, to identify the corresponding nanocrystalline domains in the TEM images. The nanocrystalline domains with different crystalline orientation in the

https://doi.org/10.1038/s41560-023-01255-2

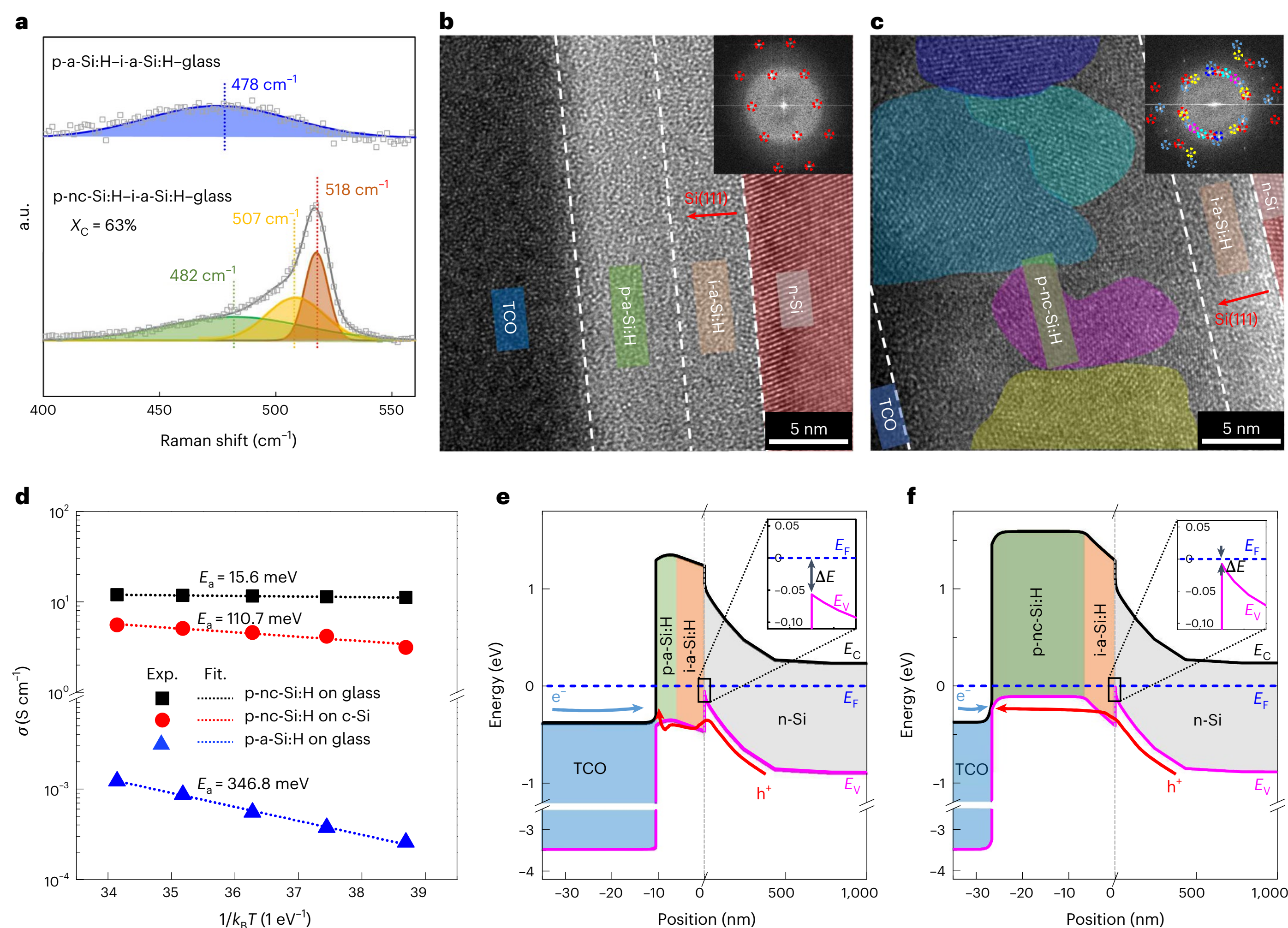

Fig. 3 | Electrical and microstructure characterizations as well as band alignment analysis of HSCs based on p-a-Si:H and p-nc-Si:H. a, Raman spectra collected from p-a-Si:H–i-a-Si:H–glass and p-nc-Si:H–i-a-Si:H–glass samples. Gaussian fitting (colour shaded areas) was implemented on the characteristic peaks at 478 cm^{-1} (a-Si:H) and at 507 and 518 cm^{-1} (nc-Si:H)[42,43]. The X_C was calculated by equation (1). **b**,**c**, TEM images of TCO–p-a-Si:H–i-a-Si:H–n-Si (**b**) and TCO–p-nc-Si:H–i-a-Si:H–n-Si (**c**) structures. The TEM images were captured on the Si (110) cross-section, and the corresponding FFT images (insets) were mathematically obtained. Crystallites in p-nc-Si:H with different orientation are distinguished by colour, and the corresponding reciprocal spots in FFT images are highlighted with coloured circles. The red arrows depict the growth direction of the silicon thin films on the Si (111) plane. **d**, Extraction of E_a for p-nc-Si:H and p-a-Si:H films without light soaking following equation (2) (dotted lines)[49]. **e**,**f**, Equilibrium band diagrams of HSCs based on p-a-Si:H (**e**) and p-nc-Si:H (**f**) related to the cross-sectional structures in **b** and **c**. E_C, E_V and E_F denote conduction band energy, valence band energy and Fermi level, respectively. Insets: enlarged view of the black wire frames; there, ΔE equals the difference between E_F and E_V at the i-a-Si:H–n-Si interface. The collection path of holes across the heterojunction is depicted as a more complicated curve (red arrows) for p-a-Si:H to illustrate a more challenging transport mechanism at the relative interfaces, with respect to the p-nc-Si:H counterpart. Current is generated once the holes meet and recombine with the electrons (along blue arrows) at the interface of the TCO–hole transport layer.

amorphous context are labelled with different background colours, and the corresponding reciprocal spots in the FFT image are circled in the same colours. A large fraction of nanocrystalline domains is observed in the p-nc-Si:H layer, while the amorphous structure of the i-a-Si:H layer is completely intact, ensuring a well-passivated and contacted silicon surface. In practice, the growth of the p-nc-Si:H layer on i-a-Si:H film is a great technical challenge, especially for high-efficiency devices, where the crystalline phase should be localized within a thin layer to balance out detrimental parasitic absorption and resistive transport. Here, the strategy for highly crystalline p-nc-Si:H involves fast nucleation at the initial stage, which was facilitated by CO_2 plasma treatment on its underlying i-a-Si:H layer[47,48], and selective removal of the amorphous fraction by the plasma with high hydrogen dilution. This led to the accumulation of dense crystallites into the a-Si:H matrix[28].

Apart from the X_C, electrical characteristics such as σ and E_a can reflect the quality of doped films. As shown in Fig. 3d, the p-nc-Si:H layer on glass exhibits a high $\sigma > 3$ S cm^{-1} and a low $E_a < 16$ meV. By contrast, the p-a-Si:H layer on glass shows values of $\sigma \approx 10^{-4}$ S cm^{-1} and $E_a \approx 350$ meV, respectively. The higher σ and lower E_a values are thus obtained from the p-nc-Si:H layer. We computed E_a from the equation

$$\sigma = \sigma_0 \exp\left(-E_a/k_B T\right), \tag{2}$$

where k_B is the Boltzmann constant and T is the temperature in kelvin[49]. The values of E_a for p-type semiconductors describe the energy difference between the Fermi level and the valence band maximum. A lower E_a in the p-nc-Si:H layer, therefore, indicates higher effective doping and work function. Note that the test films are deposited on two types of substrates (SiO_2-coated textured silicon wafer and planar glass) using the same deposition processes. Correspondingly, the deposited p-nc-Si:H layer on glass is about 1.7 times thicker than the layer grown on the pyramidal textured surface of c-Si wafer. Considering

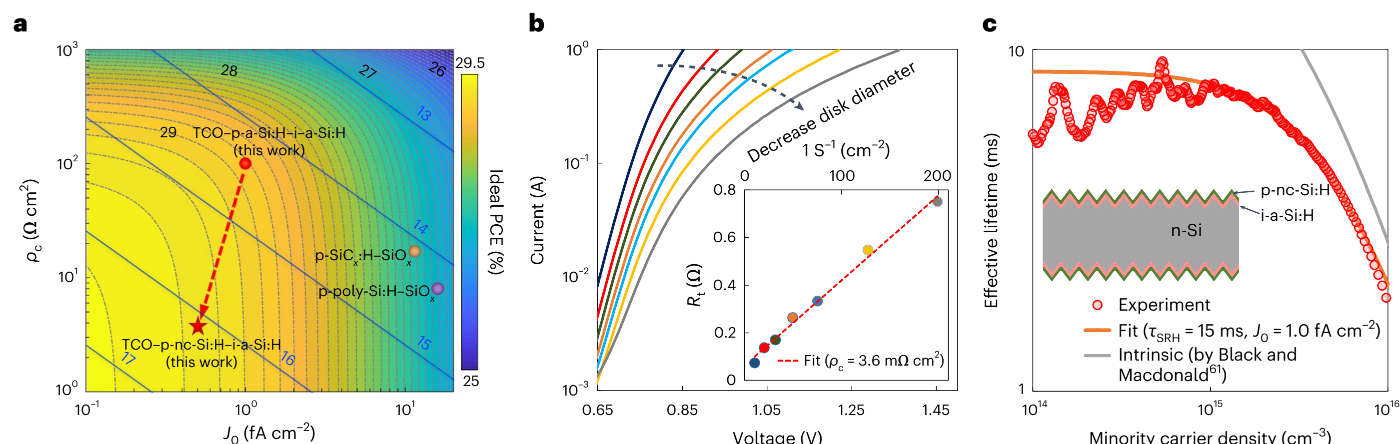

Fig. 4 | Evaluation of the carrier selectivity of HSCs based on a p-nc-Si:H layer. **a**, Plot of ideal PCE as a function of contact resistivity ρ_c and recombination current density J_0 for different HSCs, assuming a 110-µm-thick undoped c-Si bulk and J_{sc} of 43.31 mA cm^{-2} per Richter's limiting efficiency model. Blue lines (with blue numbers) represent the selectivity S_{10} according to ref. 53, while dashed–dotted lines (with black numbers) are the contour lines for ideal PCE. Several typical HSCs, including p-a-Si:H (this work; red circle), p-nc-Si:H (this work; red star), p-SiC$_x$:H (ref. 7; yellow circle) and p-poly-Si:H (refs. 55,56; purple circle) are marked for comparison. **b**,**c**, Experimental measurements of ρ_c by ECSM[58,59] (**b**) and J_0 by Sinton WCT-120 (**c**) for HSC based on p-nc-Si:H (ref. 6). Inset (**b**): the total series resistances (R_t) from different disks plotted against inverse area (1 S^{-1}). The ρ_c of 3.6 mΩ cm^2 is extracted by linear fitting (dashed line). Inset (**c**): the passivated sample with a symmetrical structure used for the J_0 test; τ_{SRH} and J_0 are estimated as 15 ms and 1.0 fA cm^{-2}, respectively, according to the methods from ref. 5 (here, the grey line indicating intrinsic lifetime, τ_{intr}, is taken from ref. 61).

the thickness sensitivity of X_C and E_a[31], the much smaller E_a value of the p-nc-Si:H layer on glass than that on the c-Si wafer is caused by variations in the thickness-dependent crystallization fraction. It should also be noted that the above tests are on samples without light soaking; the E_a plots of the samples under light soaking are shown in Supplementary Fig. 4. With light soaking, the E_a and σ values of both films are slightly improved, except for the σ of p-a-Si:H; this increases by a factor of two to three. Although light soaking is used in final devices, it occurs at the front side of the solar cell. Thus, we assume that the properties of HSCs at the rear side are negligibly influenced, and the p-a-Si:H- and p-nc-Si:H-layer properties without light soaking should approximate conditions seen by real devices.

To evaluate the real device performance more accurately, we chose E_a values of 110.7 meV (346.8 meV) for p-nc-Si:H (p-a-Si:H) tested on textured silicon wafers as input parameters for simulated band diagrams. Here, to fit the tested I–V curves in Supplementary Fig. 5, the simulated I–V curves in Supplementary Fig. 6 were carefully regulated by adjusting the simulation parameters so that the accuracy of the technology computer-aided design (TCAD) simulated band diagrams shown in Fig. 3e,f is ensured. The p-layer change leads to adjustments from three aspects: (1) conductivity of the p layer itself, (2) band bending at the c-Si surface and (3) carrier transport at the TCO–p-layer interface. All the three aspects have favourable influences on minimizing resistive losses in the HSC and consequently, yielding maximal FF in the devices. The relevant interpretation is elaborated as follows.

First, the p-nc-Si:H layer presents a much higher dark conductivity than the p-a-Si:H layer, which is beneficial for reducing resistive loss in the p layer itself. Second, compared with the p-a-Si:H case, the p-nc-Si:H layer has favourable band bending at the c-Si surface region. This is reflected by the smaller gap between the valence band maximum and the Fermi level (ΔE) (insets in Fig. 3e,f). The reason for this is the lower E_a, hence higher work function, of the p-nc-Si:H sample. The accumulation of holes at the surface of n-Si for the p-nc-Si:H sample is also much higher than that of the p-a-Si:H case, leading to a larger difference between hole and electron concentrations and thus, an improvement in electrical passivation. Moreover, this enhanced band bending at the p layer–i layer–n-Si stack provides a lower and sharper energy barrier, which favours a collection of holes through tunnelling at the HSC. Accordingly, lower J_0 and ρ_c in the p layer–i layer–n-Si stack is obtained. Third, holes in the p-layer valence band recombine with electrons in the TCO conduction band. As elaborated by Procel et al.[50,51], the ρ_c variations at the interface are linked to the dominating carrier transport mechanisms and can be influenced by the energy alignment of the p layer–TCO contact. The p-nc-Si:H–TCO interface features a lower hole transport barrier than the p-a-Si:H–TCO case, as indicated in Fig. 3e,f. According to Fig. 3f, the energy alignment at the p-nc-Si:H–TCO interface could facilitate carrier transport through dominating BTBT, which is widely considered to be the most efficient carrier transport mechanism. By contrast, at the p-a-Si:H–TCO interface, trap-assisted tunnelling, which is usually a less efficient tunnelling mechanism than BTBT, is likely to dominate; this is confirmed by our simulated results in Fig. 3e. Therefore, a higher ρ_c at the p-a-Si:H–TCO interface is to be expected. It should be mentioned that the band gap of p-nc-Si:H (~1.7–2 eV) is simplified to be consistent with that of i-a-Si:H because it has little effect on the simulation result (J–V) if the E_a of the doped layer is small enough[50–52].

Evaluation of holes selectivity

The replacement of the p-a-Si:H layer with a p-nc-Si:H layer improves the passivation quality and reduces ρ_c values at both the p layer–i-a-Si:H–n-Si contact and the TCO–p layer interface. These positive effects contribute to delivering a larger hole selectivity of the HSCs. Figure 4a shows the distributions of simulated solar cell efficiency and hole selectivity as functions of ρ_c and J_0. We extract ρ_c and J_0 of HSCs based on p-nc-Si:H directly from the measurements shown in Fig. 4b,c, while those of p-a-Si:H are evaluated according to the fitting parameters in Fig. 2 and Supplementary Fig. 1. The selectivity values are indicated by the blue lines, with $S_{10} = \log_{10}[V_{th}/(J_0 \times \rho_c)]$ (refs. 53,54). For comparison, the S_{10} values of several typical HSCs with p layers of p-a-Si:H, p-SiC$_x$:H and p-poly-Si:H are also included. As shown in Fig. 4a, from the top right corner to the bottom left corner of the plot, solar cell efficiency increases with the increase of S_{10} from 13 to 17. The solar cell with a p-nc-Si:H layer features $S_{10} > 16$, which is higher than solar cells using the p-a-Si:H (this work), p-SiC$_x$:H (ref. 7) and p-poly-Si:H layers[55,56]. Provided that an ideal ESC and our p-nc-Si:H HSC are considered, the theoretical PCE of the resultant SHJ solar cells could reach up to 29.2%.

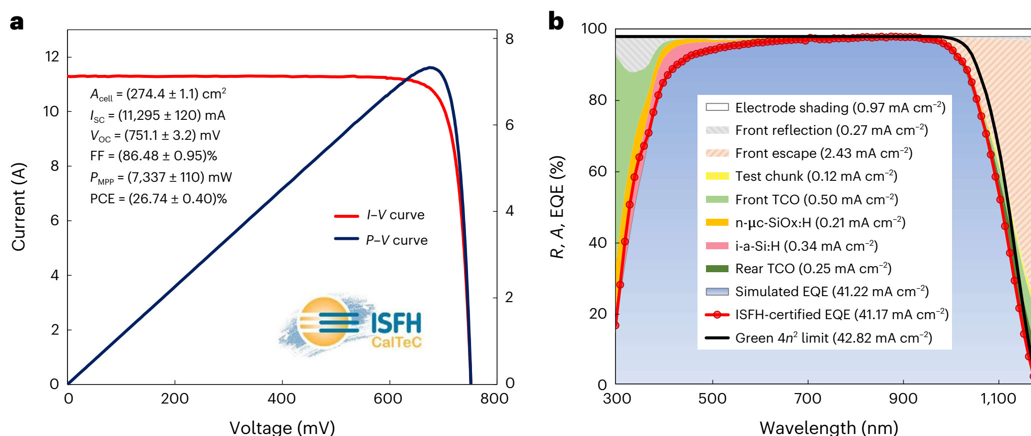

Fig. 5 | Certified SHJ solar cell with a PCE of 26.74%. a, Light *I*–*V* and power–voltage (*P*–*V*) curves of the record front–back contact silicon solar cell. **b**, External quantum efficiency (EQE) spectrum and analysis of the optical loss, including reflection (*R*) and absorption (*A*). The maximal EQE (Green $4n^2$ limit[72]) for 130-μm-thick n-Si excluding electrode shading is also reported for comparison.

Three methods—the Cox and Strack method (CSM)[57], the expanded Cox and Strack method (ECSM)[58,59] and the transfer length method (TLM)[60]—were utilized to extract the ρ_c of HSCs based on p-nc-Si:H. Emphasis was placed on the ECSM, which can directly extract the ρ_c values of the TCO–p-nc-Si:H–i-a-Si:H–n-Si stack, as shown in Fig. 4b. The other two methods, which evaluate the ρ_c through measuring symmetric samples on a p-type silicon wafer (p-Si), are shown in Supplementary Fig. 7. The coloured lines in Fig. 4b are the dark current–voltage (dark *I*–*V*) curves of the ECSM disks with different diameters (the same as the CSM disks shown in Supplementary Fig. 7a but with the n-Si wafer as the substrate). The inset in Fig. 4b shows total series resistance (R_t) from different disks plotted against inverse area ($1\,S^{-1}$). From the linear fit (red dashed line), we can extract a ρ_c of 3.6 mΩ cm². For comparison, the results extracted from CSM and TLM are 4.2 and 6.5 mΩ cm², respectively.

A symmetric structure, shown in the inset of Fig. 4c, was used to characterize J_0 for the HSC based on p-nc-Si:H. The transient mode of a Sinton measurement was used for testing minority carrier lifetime, and the results are indicated by red circles. The intrinsic recombination mode presented by Black and Macdonald[61] was used to fit the data, tuning the parameters of SRH recombination (τ_{SRH}; reflecting the quality of silicon wafer) and J_0 (representing the quality of surface passivation). The fitted total J_0 is 1.0 fA cm^{-2}. Considering the symmetry of the structure, it should be 0.5 fA cm^{-2} for the J_0 of the p-nc-Si:H–i-a-Si:H–n-Si HSC.

The achievements in electrical performance of the p-nc-Si:H cell (26.30% PCE) define a state-of-the-art SHJ process on which advanced optical designs can be adopted to further promote PCE. As shown in Fig. 5a, with the same BJ processing as the p-nc-Si:H cell, reducing the shading ratio from 2.8 to 2.0% after using the laser transfer process and modifying the window layers of n-nc-SiO$_x$:H, i-a-Si:H and TCO at the front (such as reducing the thickness of n-nc-SiO$_x$:H and i-a-Si:H, increasing the oxygen content of n-nc-SiO$_x$:H and decreasing the carrier density of TCO) to minimize the parasitic absorption, we achieved a higher PCE of 26.74% with the increase of J_{SC} to 41.16 mA cm^{-2}. The slight reduction of FF is mainly due to the change of front metal fingers. In addition, V_{OC} increases by 0.9 mV, possibly enhanced by the higher J_{SC}. The external quantum efficiency spectrum and main optical loss of each layer are shown in Fig. 5b. The absorption by n-Si fits well with the Institute for Solar Energy Research in Hamelin (ISFH)-certified one, and the slight deviation at short wavelength may arise from the refractive indices used in the simulation. The front grid electrode causes a decrease of 0.97 mA cm^{-2} in J_{SC}, accounting for a shading fraction of 2.0%. In the ultraviolet range, the front TCO, n-nc-SiO$_x$:H and i-a-Si:H dominate the loss due to parasitic absorption. In the near-infrared range, the major source of loss is the escape of light from the front, which is attributed to reflection by the test chunk due to the limited wafer thickness. With introducing an additional reflective MgF$_2$/Ag stack at the rear side and regulating the transmittance of TCO, the J_{SC} was further improved to 41.45 mA cm^{-2} due to the optical gain, while FF decreased to 86.07% due to the decrease of TCO conductivity. Finally, the PCE was improved to 26.81%. The certified *J*–*V* curve of the device is reported in Supplementary Fig. 8.

Conclusion

Through introducing nanocrystallization technology in the doped layer at carrier-selective contacts for both polarities, we achieve a record efficiency of 26.81% and on a different cell, an extremely high FF (86.59%) on M6-sized BJ SHJ solar cells. Two types of SHJ solar cells equipped with p-type transporting layers of amorphous silicon and nanocrystalline silicon are comprehensively investigated; we study their power loss, contact resistivity, transport mechanism and so on. Structural and electrical characterizations of the boron-doped nanocrystalline silicon films indicate that a higher X_C (>63%), an increase in conductivity of four orders of magnitude (in comparison with p-type amorphous silicon) and an ultralow E_a (<115 meV) are the main causes of its excellent electrical performance. Because of the low E_a of p-nc-Si:H, it is easy to enable BTBT at the n-type TCO–p-nc-Si:H interface and achieve sharp band bending at the i-a-Si:H–n-Si interface, facilitating efficient transport and collection of holes across the whole junction. Our study shows that the implementation of p-nc-Si:H together with a modified TCO greatly reduces the contact resistivity of HSC, from >100 to <5 mΩ cm². The total series resistance of the solar cell is reduced from the original 0.37 to 0.2 Ω cm², yielding a record FF for single-junction silicon solar cell.

Methods

Solar cell fabrication

In this work, solar cells were fabricated by the commercial SHJ research and development line on LONGi M2 (the 25.26% efficiency SHJ solar cell) or on an M6 Czochralski n-Si wafer with a resistivity of 1.2–1.5 Ω cm and a thickness of 130 μm in (100) orientation. The n-Si wafer was first cleaned and textured by a wet chemical process. Before subsequent deposition, the thickness of the n-Si wafer was confirmed by weight measurement. Radiofrequency plasma-enhanced chemical vapour deposition was used to prepare i-a-Si:H, and then, very high-frequency plasma-enhanced chemical vapour deposition (40.68 MHz) systems

https://doi.org/10.1038/s41560-023-01255-2

were used to deposit n-nc-SiO_x:H, p-a-Si:H and p-nc-Si:H layers during the device fabrication. For the i-a-Si:H–n-Si interface of the 25.26% cell, an ultrathin 0.5- to 1.0-nm buffer layer, rich in H content, was introduced to improve the passivation.[12] While for that of 26.30, 26.74 and 26.81% cells, an O-terminated Si surface, grown by a self-limiting wet chemical oxidation process (using HF/H_2O_2 solution), was introduced to suppress Si epitaxy[62–64]. Before deposition of p-nc-Si:H, CO_2 plasma treatment was carried out on i-a-Si:H, which forms a thin barrier layer for impeding the damage. Supplementary Table 6 shows the detail parameters of the growth process for doped layers. The TCO layers used in 25.26% cells were prepared by direct current sputtering with rotationally target, while the updated TCO layers used in 26.30, 26.74 and 26.81% cells were grown by the reactive plasma deposition technique. The material of the updated TCO is 1 wt% CeO_2 doped In_2O_3, while that of original TCO is SCOT (name of commodity; manufactured by Advanced Nano Products) for the front side and conventional 10 wt% SnO_2 doped In_2O_3 for the rear side of the device. Silver grid electrodes were printed followed by annealing at 190 °C for 30 min. With the improvement of the metallization process, the metal fraction of the front electrode for different SHJ solar cells decreased from 3.2 to 2.0%, while the rear electrode patterning with fingers and bus bars remained basically unchanged. For the above situation of 2.0% metal fraction, laser transfer process was introduced to make the front finger. To further increase J_{SC}, a 150-nm-thick MgF_2 film was evaporated on the front TCO layer as a second antireflective coating. For 26.81% cell, an additional 120-nm-thick MgF_2/150-nm-thick Ag stack was evaporated on the rear TCO layer, which means this cell is a monofacial solar cell. Finally, light soaking under 60 suns was carried out for 90 s at 190 °C.

PLA

Two methods were utilized for the PLA of the solar cells with PCEs of 25.26% (p-a-Si:H cell) and 26.30% (p-nc-Si:H cell). One is based on Quokka2 software (as shown in Fig. 2), and the other is referring to a simple recombination model (as shown in Supplementary Fig. 1). For the Quokka2 simulation, the unit cell was modelled in two dimensions to calculate the power loss in the transversal transport of carriers between two fingers. The input parameters were primarily obtained from measurements 'Characterizations'. The line resistance of the finger and the contact resistivity of the heterojunction were considered as series resistance in an external circuit. The optical path-length factor (Z) was set as $4n^2$, and the transmittance was adjusted to match the simulated J_{SC} to that of actual cells. The τ_{SRH} of the silicon wafers was set by adjusting the values of σ_n, σ_p and the defect density of the SRH defect (N_t). τ_{SRH}, J_{01} (surface recombination) and R_s were further tuned to obtain agreement between the light J–V and the Suns–V_{OC} curves. Richter's Auger mode was chosen, and the value of radiation recombination was changed to $0.4 \times B_{rad}$ with a photon recycling probability of 0.6 (ref. 65). Other parameters in the simulation are listed in Supplementary Table 4. It should be noted that since band gap narrowing is not considered in this model, the corresponding V_{OC} may deviate somewhat from the experimental value. For the simulation by the simple recombination model method, we first assume a uniform quasi-Fermi level and then fit the Suns–V_{OC} and light J–V curves by adding the formulas of intrinsic recombination, SRH recombination, surface recombination, series resistance and so on. The specific fitting parameters, consequent results and corresponding descriptions are shown in Supplementary Discussion 1 and Supplementary Fig. 1.

Electrical simulation

The band diagrams in Fig. 3e,f and the dark I–V curves in Supplementary Fig. 6 were calculated by using Sentaurus TCAD based on drift-diffusion models. The simulation structure of the testing device is illustrated in Supplementary Fig. 7a but with n-Si as the substrate: that is, a stacked film of Ag–TCO–p-nc-Si:H (or p-a-Si:H)–i-a-Si:H on bulk n-Si with a disk shape on the front surface and a full-area ohmic contact on the rear surface of the n-Si substrate. Physical models, including surface recombination, Auger recombination in substrate and thermionic emission at proper interfaces, are taken into consideration. Moreover, p-a-Si:H and p-nc-Si:H layers feature spatially uniformly distributed traps in the exponential and Gaussian energy distributions[50]. Trap-assisted tunnelling and BTBT models are also considered at the TCO–p-nc-Si:H (or p-a-Si:H) interface. The specific film parameters are shown in Supplementary Table 7. The simulated results are consistent with the experiments (Supplementary Figs. 5 and 6 and Supplementary Discussion 2).

Optical simulation

The optical simulation in Fig. 5b was performed using the SunSolve software provided by PV Lighthouse. In the simulation, we use refractive indices from the literature[66–70] except for the TCO film, which we measured by ellipsometry. In SunSolve, ray tracing and thin-film optics were adopted with a Monte Carlo algorithm for sampling and averaging the absorption in each layer. Here, 1 million rays with zero zenith angle and air mass 1.5G were randomly generated for better confidence of the statistics; the 95% confidence interval of cell absorption is less than 0.01 mA cm^{-2}.

Characterizations

The light J–V curves of the solar cells were tested and certified by ISFH (Supplementary Fig. 8); gold-coated brass chuck was used to mount the solar cells, and the resistance of the grid at the rear side and of bus bars at the front side was neglected. The pseudo light J–V curves were extracted from a Suns–V_{OC} measurement. The Suns–V_{OC} module of a Sinton WCT-120 instrument was used to collect the changes in voltage of the device by reducing the light intensity of the flashlight; these were computationally transformed them into Suns–V_{OC} curves. Raman spectra were obtained with a Horiba LabRAM Odyssey Raman spectrometer with a 325-nm excitation laser. Test films were deposited on cleaned glass substrates using the same deposition processes as the solar cells. The morphology of heterojunctions, consisting of TCO-coated doped amorphous and nanocrystalline silicon films on c-Si bulk, was observed by TEM, and the test samples were prepared by the focused ion beam method. Activation energies were calculated from measurements of electrical conductivity as a function of test temperature. Electrical conductivities were calculated from I–V curves measured by a semiconductor analyser (Keithley 4200A-SCS). It should be noted that the 50-nm isolation layer of SiO_x film was deposited by plasma-enhanced chemical vapour deposition before the deposition of p-nc-Si:H or p-a-Si:H on the pyramid-textured silicon wafers. Contact resistivity tests were carried out using the CSM, ECSM and TLM; the details are shown in Fig. 4b and Supplementary Fig. 7. Sinton's minority carrier lifetime test was used to characterize the passivation quality on a symmetric structure of p-nc-Si:H–i-a-Si:H–n-Si–i-a-Si:H–p-nc-Si:H (Fig. 4c). The transient mode of a Sinton measurement was used for testing the minority carrier lifetime. Pyramid-textured n-Si wafers with a thickness of about 130 μm and resistivity of about 1.59 Ω cm were used as the substrates.

Reporting summary

Further information on research design is available in the Nature Portfolio Reporting Summary linked to this article.

Data availability

All data generated or analysed during this study are included in the published article and its Supplementary Information. Source data are provided with this paper.

References

1. Min, B., Müller, M., Wagner, H., Fischer, G. & Brendel, R. A roadmap toward 24% efficient PERC solar cells in industrial mass production. *IEEE J. Photovolt.* **7**, 1541–1550 (2017).

2. Green, M. A. The passivated emitter and rear cell (PERC): from conception to mass production. *Sol. Energy Mater. Sol. Cells* **143**, 190–197 (2015).
3. Richter, A. et al. Design rules for high-efficiency both-sides-contacted silicon solar cells with balanced charge carrier transport and recombination losses. *Nat. Energy* **6**, 429–438 (2021).
4. Haase, F. et al. Laser contact openings for local poly-Si-metal contacts enabling 26.1%-efficient POLO-IBC solar cells. *Sol. Energy Mater. Sol. Cells* **186**, 184–193 (2018).
5. Yoshikawa, K. et al. Silicon heterojunction solar cell with interdigitated back contacts for a photoconversion efficiency over 26%. *Nat. Energy* **2**, 17032 (2017).
6. Yoshikawa, K. et al. Exceeding conversion efficiency of 26% by heterojunction interdigitated back contact solar cell with thin-film Si technology. *Sol. Energy Mater. Sol. Cells* **173**, 37–42 (2017).
7. Khler, M. et al. A silicon carbide-based highly transparent passivating contact for crystalline silicon solar cells approaching efficiencies of 24%. *Nat. Energy* **6**, 529–537 (2021).
8. Wolf, S. D., Descoeudres, A., Holman, Z. C. & Ballif, C. High-efficiency silicon heterojunction solar cells: a review. *Green* **2**, 7–24 (2012).
9. Herasimenka, S. Y., Dauksher, W. & Bowden, S. G. >750 mV open-circuit voltage measured on 50-μm-thick silicon heterojunction solar cell. *Appl. Phys. Lett.* **103**, 053511 (2013).
10. Taguchi, M., Yano, A., Tohoda, S., Matsuyama, K. & Maruyama, E. 24.7% record efficiency HIT solar cell on thin silicon wafer. *IEEE J. Photovolt.* **4**, 96–99 (2014).
11. Li, H. et al. The amorphous/crystalline silicon interface research of HIT solar cells by simulation. *Adv. Mat. Res.* **773**, 124–131 (2013).
12. Ru, X., Qu, M., Wang, J., Ruan, T. & Xu, X. 25.11% efficiency silicon heterojunction solar cell with low deposition rate intrinsic amorphous silicon buffer layers. *Sol. Energy Mater. Sol. Cells* **215**, 110643 (2020).
13. Qu, X. et al. Identification of embedded nanotwins at c-Si/a-Si:H interface limiting the performance of high-efficiency silicon heterojunction solar cells. *Nat. Energy* **6**, 194–202 (2021).
14. Street, R. A., Biegelsen, D. K. & Knights, J. C. Defect states in doped and compensated a-Si:H. *Phys. Rev. B* **24**, 969–984 (1981).
15. Bivour, M., Reichel, C., Hermle, M. & Glunz, S. W. Improving the a-Si:H(p) rear emitter contact of n-type silicon solar cells. *Sol. Energy Mater. Sol. Cells* **106**, 11–16 (2012).
16. Messmer, C., Bivour, M., Luderer, C., Tutsch, L. & Hermle, M. Influence of interfacial oxides at TCO/doped Si thin film contacts on the charge carrier transport of passivating contacts. *IEEE J. Photovolt.* **10**, 343–350 (2019).
17. Gogolin, R. et al. Analysis of series resistance losses in a-Si:H/c-Si heterojunction solar cells. *IEEE J. Photovolt.* **4**, 1169–1176 (2014).
18. Liu, W. et al. Light-induced activation of boron doping in hydrogenated amorphous silicon for over 25% efficiency silicon solar cells. *Nat. Energy* **7**, 427–437 (2022).
19. Luderer, C., Messmer, C., Hermle, M. & Bivour, M. Transport losses at the TCO/a-Si:H/c-Si heterojunction: influence of different layers and annealing. *IEEE J. Photovolt.* **10**, 952–958 (2020).
20. Ghahfarokhi, O. M., Maydell, K. V. & Agert, C. Enhanced passivation at amorphous/crystalline silicon interface and suppressed Schottky barrier by deposition of microcrystalline silicon emitter layer in silicon heterojunction solar cells. *Appl. Phys. Lett.* **104**, 113901 (2014).
21. Seif, J. P. et al. Strategies for doped nanocrystalline silicon integration in silicon heterojunction solar cells. *IEEE J. Photovolt.* **6**, 1132–1140 (2016).
22. Sharma, M., Panigrahi, J. & Komarala, V. K. Nanocrystalline silicon thin-film growth and application for silicon heterojunction solar cells: a short review. *Nanoscale Adv.* **3**, 3373–3383 (2021).
23. Strahm, B., Howling, A. A., Sansonnens, L. & Hollenstein, C. Plasma silane concentration as a determining factor for the transition from amorphous to microcrystalline silicon in SiH_4/H_2 discharges. *Plasma Sources Sci. Technol.* **16**, 80–89 (2007).
24. Finger, F. et al. Improvement of grain size and deposition rate of microcrystalline silicon by use of very high frequency glow discharge. *Appl. Phys. Lett.* **65**, 2588–2590 (1994).
25. Zhao, Y. et al. Doped hydrogenated nanocrystalline silicon oxide layers for high-efficiency c-Si heterojunction solar cells. *Prog. Photovolt.* **28**, 425–435 (2020).
26. Mazzarella, L. et al. Nanocrystalline silicon emitter optimization for Si-HJ solar cells: substrate selectivity and CO_2 plasma treatment effect. *Phys. Status Solidi A* **214**, 1532958 (2017).
27. Umishio, H., Sai, H., Koida, T. & Matsui, T. Nanocrystalline-silicon hole contact layers enabling efficiency improvement of silicon heterojunction solar cells: impact of nanostructure evolution on solar cell performance. *Prog. Photovolt. Res. Appl.* **29**, 344–356 (2021).
28. Fioretti, A. N., Boccard, M., Monnard, R. & Ballif, C. Low-temperature p-type microcrystalline silicon as carrier selective contact for silicon heterojunction solar cells. *IEEE J. Photovolt.* **9**, 1158–1165 (2019).
29. Boccard, M. et al. Hole-selective front contact stack enabling 24.1%-efficient silicon heterojunction solar cells. *IEEE J. Photovolt.* **11**, 9–15 (2020).
30. Sai, H., Umishio, H. & Matsui, T. Very thin (56 μm) silicon heterojunction solar cells with an efficiency of 23.3% and an open-circuit voltage of 754 mV. *Sol. RRL* **5**, 2100634 (2021).
31. Zhao, Y. et al. Design and optimization of hole collectors based on nc-SiO_x:H for high-efficiency silicon heterojunction solar cells. *Sol. Energy Mater. Sol. Cells* **219**, 110779 (2021).
32. Mazzarella, L., Morales-Vilches, A. B., Hendrichs, M., Kirner, S. & Stannowski, B. Nanocrystalline n-type silicon oxide front contacts for silicon heterojunction solar cells: photocurrent enhancement on planar and textured substrates. *IEEE J. Photovolt.* **8**, 70–78 (2017).
33. Mazzarella, L. et al. p-type microcrystalline silicon oxide emitter for silicon heterojunction solar cells allowing current densities above 40 mA/cm^2. *Appl. Phys. Lett.* **106**, 023902 (2015).
34. Thomas, G., Allen, J. B., Yang, X., Javey, A. & De Wolf, S. Passivating contacts for crystalline silicon solar cells. *Nat. Energy* **4**, 914–928 (2019).
35. Chen, Y. et al. Mass production of industrial tunnel oxide passivated contacts (TOPCon) silicon solar cells with average efficiency over 23% and modules over 345 W. *Prog. Photovolt. Res. Appl.* **27**, 827–834 (2019).
36. Green, M. A. Solar cell fill factors: general graph and empirical expressions. *Solid-State Electron.* **24**, 788–789 (1981).
37. LONGi breaks three more world records for solar cell efficiency. *LONGi* https://www.longi.com/en/news/7474/ (2021).
38. Quokka 2 (PV Lighthouse, 2016).
39. Fell, A. A free and fast three-dimensional/two-dimensional solar cell simulator featuring conductive boundary and quasi-neutrality approximations. *IEEE Trans. Electron Devices* **60**, 733–738 (2013).
40. Han, C. et al. Towards bifacial silicon heterojunction solar cells with reduced TCO use. *Prog. Photovolt.* **30**, 750–762 (2022).
41. Pysch, D., Mette, A. & Glunz, S. W. A review and comparison of different methods to determine the series resistance of solar cells. *Sol. Energy Mater. Sol. Cells* **91**, 1698–1706 (2007).
42. Xia, H. et al. Phonon mode study of Si nanocrystals using micro-Raman spectroscopy. *J. Appl. Phys.* **78**, 6705–6708 (1995).
43. Zhang, S. et al. The diphasic nc-Si/a-Si:H thin film with improved medium-range order. *J. Non Cryst. Solids* **338**, 188–191 (2004).

44. Bustarret, E., Hachicha, M. A. & Brunel, M. Experimental determination of the nanocrystalline volume fraction in silicon thin films from Raman spectroscopy. *Appl. Phys. Lett.* **52**, 1675–1677 (1988).
45. Fathi, E. V., Vieira, Y. & Sazonov, M. Boron-doped nanocrystalline silicon thin films for solar cells. *Appl. Surf. Sci.* **257**, 8901–8905 (2011).
46. Voutsas, A. T., Hatalis, M. K., Boyce, J. & Chiang, A. Raman spectroscopy of amorphous and microcrystalline silicon films deposited by low-pressure chemical vapor deposition. *J. Appl. Phys.* **78**, 6999–7006 (1995).
47. Boccard, M., Monnard, R., Antognini, L. & Ballif, C. Silicon oxide treatment to promote crystallinity of p-type microcrystalline layers for silicon heterojunction solar cells. In *The 8th International Conference on Crystalline Silicon Photovoltaics* https://doi.org/10.1063/1.5049266 (AIP, 2018).
48. Yang, Y. et al. n-type nc-SiO_x:H film enables efficient and stable silicon heterojunction solar cells in sodium environment. *Mater. Lett.* **309**, 131360 (2022).
49. Nie, G. Z. N., Zhong, C. L., Luo, L. E. & Xu, Y. A modification of usual *C–V* measurement to more precisely characterize the band offsets in a-Si:H/c-Si heterojunctions. *Results Phys.* **5**, 286–289 (2015).
50. Procel, P. et al. The role of heterointerfaces and subgap energy states on transport mechanisms in silicon heterojunction solar cells. *Prog. Photovolt. Res. Appl.* **28**, 935–945 (2020).
51. Procel, P., Yang, G., Isabella, O. & Zeman, M. Theoretical evaluation of contact stack for high efficiency IBC-SHJ solar cells. *Sol. Energy Mater. Sol. Cells* **186**, 66–77 (2018).
52. Biron, R. et al. Window layer with p doped silicon oxide for high V_{oc} thin-film silicon n–i–p solar cells. *J. Appl. Phys.* **110**, 1081–1842 (2011).
53. Brendel, R. & Peibst, R. Contact selectivity and efficiency in crystalline silicon photovoltaics. *IEEE J. Photovolt.* **6**, 1413–1420 (2016).
54. Brendel, R., Riencker, M. & Peibst, R. A quantitative measure for the carrier selectivity of contacts to solar cells. In *32nd European Photovoltaic Solar Energy Conference & Exhibition* 447–451 (WIP, 2016).
55. Yan, D., Cuevas, A., Wan, Y. & Bullock, J. Passivating contacts for silicon solar cells based on boron-diffused recrystallized amorphous silicon and thin dielectric interlayers. *Sol. Energy Mater. Sol. Cells* **152**, 73–79 (2016).
56. Jan, S., Robby, P. & Rolf, B. Surface passivation of crystalline silicon solar cells: present and future. *Sol. Energy Mater. Sol. Cells* **187**, 39–54 (2018).
57. Cox, R. H. & Strack, H. A. Ohmic contacts for GaAs devices. *Solid State Electron.* **10**, 1213–1218 (1966).
58. Wang, W. et al. An expanded Cox and Strack method for precise extraction of specific contact resistance of transition metal oxide/n-silicon heterojunction. *IEEE J. Photovolt.* **9**, 1113–1120 (2019).
59. Chen, L. et al. Realization of a general method for extracting specific contact resistance of silicon-based dopant-free heterojunctions. *Sol. RRL* **6**, 2100394 (2021).
60. Reeves, G. K. & Harrison, H. B. Obtaining the specific contact resistance from transmission line model measurements. *IEEE Electron Device Lett.* **3**, 111–113 (2005).
61. Black, L. E. & Macdonald, D. H. On the quantification of Auger recombination in crystalline silicon. *Sol. Energy Mater. Sol. Cells* **234**, 111428 (2022).
62. Eom, D. H., Kim, K. S. & Park, J. G. Passivation and etching of wafer surfaces in HF–H_2O_2–IPA solutions. *Jpn J. Appl. Phys.* **41**, 5881–5886 (2002).
63. Jayachandran, S. et al. Growth mechanisms for Si epitaxy on O atomic layers: impact of O content and surface structure. *Appl. Surf. Sci.* **384**, 152–160 (2016).
64. Koehler, M. et al. Wet-chemical preparation of silicon tunnel oxides for transparent passivated contacts in crystalline silicon solar cells. *ACS Appl. Mater. Interfaces* **10**, 14259–14263 (2018).
65. Richter, A., Hermle, M. & Glunz, S. W. Reassessment of the limiting efficiency for crystalline silicon solar cells. *IEEE J. Photovolt.* **3**, 1184–1191 (2013).
66. Abolmasov, S., Cabarrocas, P. R. I. & Chatterjee, P. Towards 12% stabilised efficiency in single junction polymorphous silicon solar cells: experimental developments and model predictions. *EPJ Photovolt.* **7**, 70302 (2016).
67. Dodge, M. J. Refractive properties of magnesium fluoride. *Appl. Opt.* **23**, 1980–1985 (1984).
68. Green, M. A. Self-consistent optical parameters of intrinsic silicon at 300 K including temperature coefficients. *Sol. Energy Mater. Sol. Cells* **92**, 1305–1310 (2015).
69. Nguyen, H. T., Rougieux, F. E., Mitchell, B. & Macdonald, D. Temperature dependence of the band-band absorption coefficient in crystalline silicon from photoluminescence. *J. Appl. Phys.* **115**, 1245 (2014).
70. Holman, Z. C. et al. Current losses at the front of silicon heterojunction solar cells. *IEEE J. Photovolt.* **2**, 7–15 (2012).
71. Richter, A., Werner, F., Cuevas, A., Schmidt, J. & Glunz, S. W. Improved quantitative description of Auger recombination in crystalline silicon. *Phys. Rev. B* **86**, 165202 (2012).
72. Yablonovitch, E. Statistical ray optics. *J. Opt. Soc. Am.* **72**, 1917–1983 (1982).

Acknowledgements

We thank Y. Wang, H. Deng, T. Xie, P. Li, Y. Liu, H. Chen, Y. Long, C. Li, Z. Zhang, L. Feng, J. Qian, B. Yang, B. Liu and K. Zhang for wafer optimization, sample preparation, cell fabrication and characterizations. We also thank Z. Liu and H. Tang of Sun Yat-sen University for transmission electron microscopy characterization and simulation. This work was financially supported by the National Key R&D Program of China (grants 2022YFB4200203 and 2022YFB4200200) and the National Natural Science Foundation of China (grants 62034009 and 62104268).

Author contributions

H.L., S.Y. and P.G. designed the characterization experiments, performed quokka simulation and analysed the data. M.Y. and X.R. contributed to the optimization of the transport layer. G.W. and S.Y. performed the characterization. M.Y., X.R., S.Y., F.P., C.H., M.Q., J.L., L.F. and X.X. contributed to the development of the silicon heterojunction solar cells. X.X. designed the solar cells. X.X., Z.L. and P.G. supervised the study. C.H., P.P.M. and O.I. performed TCAD simulation and theoretical support. H.L., S.Y. and P.G. designed the idea of the study. H.L. and S.Y. co-wrote the paper. All authors discussed and reviewed the manuscript.

Competing interests

The authors declare no competing interests.

Additional information

Supplementary information The online version contains supplementary material available at https://doi.org/10.1038/s41560-023-01255-2.

Correspondence and requests for materials should be addressed to Shi Yin, Pingqi Gao or Xixiang Xu.

Peer review information *Nature Energy* thanks Martin Green, Bertrand Paviet-Salomon, Rutger Schlatmann and the other, anonymous, reviewer(s) for their contribution to the peer review of this work.

https://doi.org/10.1038/s41560-023-01255-2

Reprints and permissions information is available at www.nature.com/reprints.

Publisher's note Springer Nature remains neutral with regard to jurisdictional claims in published maps and institutional affiliations.

Open Access This article is licensed under a Creative Commons Attribution 4.0 International License, which permits use, sharing, adaptation, distribution and reproduction in any medium or format, as long as you give appropriate credit to the original author(s) and the source, provide a link to the Creative Commons license, and indicate if changes were made. The images or other third party material in this article are included in the article's Creative Commons license, unless indicated otherwise in a credit line to the material. If material is not included in the article's Creative Commons license and your intended use is not permitted by statutory regulation or exceeds the permitted use, you will need to obtain permission directly from the copyright holder. To view a copy of this license, visit http://creativecommons.org/licenses/by/4.0/.

© The Author(s) 2023

nature research

Corresponding author(s): Xixiang Xu, Pingqi Gao, Shi Yin

Solar Cells Reporting Summary

Nature Research wishes to improve the reproducibility of the work that we publish. This form is intended for publication with all accepted papers reporting the characterization of photovoltaic devices and provides structure for consistency and transparency in reporting. Some list items might not apply to an individual manuscript, but all fields must be completed for clarity.

For further information on Nature Research policies, including our data availability policy, see Authors & Referees.

Experimental design

Please check: are the following details reported in the manuscript?

1. Dimensions

Item	Yes/No	Details
Area of the tested solar cells	☒ Yes ☐ No	244.53 square centimeter, 274.3 square centimeter, 274.4 square centimeter and 274.4 square centimeter; Stated in Methods , Fig.S8 and Calibration certificate.
Method used to determine the device area	☒ Yes ☐ No	The area of the calibration object is measured using an optical scanning system working in transmission mode and is traceable to a primary calibrated area standard (Calibration mark 50716-PTB-19 (FN001)), stated in Calibration certificate.

2. Current-voltage characterization

Item	Yes/No	Details
Current density-voltage (J-V) plots in both forward and backward direction	☐ Yes ☒ No	Forward direction is enough for silicon cells
Voltage scan conditions *For instance: scan direction, speed, dwell times*	☒ Yes ☐ No	One current-voltage characteristics consists of 165 voltage steps and each step takes a time of 300 ms, stated in Calibration certificate.
Test environment *For instance: characterization temperature, in air or in glove box*	☒ Yes ☐ No	Standard testing conditions (AM1.5G, 100 mW/cm², 25°C) , stated in Calibration certificate.
Protocol for preconditioning of the device before its characterization	☐ Yes ☒ No	Certified report not give this content.
Stability of the J-V characteristic *Verified with time evolution of the maximum power point or with the photocurrent at maximum power point; see ref. 7 for details.*	☐ Yes ☒ No	The layers and materials used for the solar cells are stable under standard testing conditions.

3. Hysteresis or any other unusual behaviour

Item	Yes/No	Details
Description of the unusual behaviour observed during the characterization	☐ Yes ☒ No	A hysteresis between forward and reverse measurements was not observed, stated in Calibration certificate.
Related experimental data	☐ Yes ☒ No	A hysteresis between forward and reverse measurements was not observed, stated in Calibration certificate.

4. Efficiency

Item	Yes/No	Details
External quantum efficiency (EQE) or incident photons to current efficiency (IPCE)	☒ Yes ☐ No	Fig. 5 b
A comparison between the integrated response under the standard reference spectrum and the response measure under the simulator	☒ Yes ☐ No	This is done by a WPVS reference cell measured at ISFH, stated in Calibration certificate.
For tandem solar cells, the bias illumination and bias voltage used for each subcell	☐ Yes ☒ No	They are not tandem solar cells.

5. Calibration

Item	Yes/No	Details
Light source and reference cell or sensor used for the characterization	☒ Yes ☐ No	The sun simulator is adjusted using a WPVS reference cell, stated in Calibration certificate.

Confirmation that the reference cell was calibrated and certified

☒ Yes ☐ No

The short circuit current of this reference cell was calibrated (primary standard "IV", Calibration mark 47086-PTB-21 (RD001)) under standard test conditions (1000 W/ m^2,AM1.5G reference spectrum and 25 °C), stated in Calibration certificate.

Calculation of spectral mismatch between the reference cell and the devices under test

☐ Yes ☒ No

Reference cell and the as measured cells are the same kind of devices, no spectral mismatch.

6. Mask/aperture

Size of the mask/aperture used during testing

☒ Yes ☐ No

All solar cells are conducted as total-area testing, stated in Calibration certificate.

Variation of the measured short-circuit current density with the mask/aperture area

☐ Yes ☒ No

All solar cells are conducted as total-area testing, stated in Calibration certificate.

7. Performance certification

Identity of the independent certification laboratory that confirmed the photovoltaic performance

☒ Yes ☐ No

Thee cells used in our manuscript have been independently confirmed by ISFH;

A copy of any certificate(s)
Provide in Supplementary Information

☒ Yes ☐ No

Figure S8 and Calibration certificate.

8. Statistics

Number of solar cells tested

☐ Yes ☒ No

It only shows three typical champion solar cells certified by ISFH.

Statistical analysis of the device performance

☐ Yes ☒ No

It only shows three typical champion solar cells certified by ISFH.

9. Long-term stability analysis

Type of analysis, bias conditions and environmental conditions
For instance: illumination type, temperature, atmosphere humidity, encapsulation method, preconditioning temperature

☐ Yes ☒ No

long-term stability analysis has not yet been performed